

ALICE-ANA-2014-xxx  
January 10, 2023

# Strangeness Production ( $\Lambda$ ) in Jets and Medium in p-Pb collisions at $\sqrt{s_{NN}} = 5.02$ TeV

Ryan Hannigan

1. University of Texas at Austin

Emails: ryan.hannigan@austin.utexas.edu

## Abstract

By studying strange hadrons in proton-proton, proton-nucleus, and heavy ion collisions, one can investigate strange quark production and hadron formation with respect to increasing system size. Recent measurements show an enhancement of strange particles (e.g. an increase in the  $\Lambda/\pi$  ratio) in p-Pb and high multiplicity pp collisions. In order to probe the origin of this increase, it is necessary to separate the strange particles produced in hard processes (jets) from those produced in soft processes (bulk). By examining this trend from low to high multiplicity p-Pb collisions, we are able to study the onset of this enhancement from small to large collision systems.

Two-particle jet-like angular correlations with identified strange hadrons in p-Pb collisions allow us to measure both the jet and non-jet components of strange particle production. Modifications in the production mechanisms across different system sizes can be probed by examining changes in the  $\Lambda/h$  ratio within jets and in the underlying event separately. In addition, changes to the jet hadrochemistry via medium interactions are studied by measuring strangeness production in the away-side jet. In this note we present the first measurements of the  $\Lambda/h$  ratio in jets as a function of multiplicity using jet-like hadron- $\Lambda$  angular correlations in p-Pb collisions at  $\sqrt{s_{NN}} = 5.02$  TeV.



## Contents

### 1 Introduction

Recent studies have shown that the ratio of the yield of  $\Lambda$  baryons to charged pions differs between pp, p-Pb and PbPb collisions, specifically in the mid- $p_T$  region of 1–4 GeV/c. Additionally, similar studies have seen an increase in the  $\Lambda/(\pi^+ + \pi^-)$  yields as a function of charged particle multiplicity in p-Pb collisions. The origin of this increase is still unknown.

By performing angular correlations of a high  $p_T$  trigger hadron with an associated  $\Lambda$  (or charged hadron as a proxy for a pion) in p-Pb events, we are able to separate out  $\Lambda$  baryon production into three distinct kinematic regions:

- The near-side peak of the correlation, corresponding to jet-like production with no medium interactions,
- The away-side peak of the correlation, corresponding to jet-like production with possible medium interaction, and
- The underlying event, corresponding to soft production within the medium.

For this study, 1-d  $\Delta\phi$  angular correlations of jet-like  $h - \Lambda$  and  $h - h$  pairs were measured in p-Pb events independently for three multiplicity bins (0-20%, 20-50%, 50-80%), and the final ratios of yields of correlated pairs were compared to study the onset of this enhancement. These correlations were measured using the PWGLF/Strangeness/DPhi/AliAnalysisTaskLambdaHadronRatio class.

### 2 Event and Track Selection

#### 2.1 Dataset

Every event in this analysis was a p-Pb collision at  $\sqrt{s_{NN}} = 5.02$  TeV taken from the following runlist which consists of 32 runs during the LHC16q period:

**265525, 265521, 265501, 265500, 265499, 265435, 265427, 265426, 265425, 265424, 265422, 265421, 265420, 265419, 265388, 265387, 265385, 265384, 265383, 265381, 265378, 265377, 265344, 265343, 265342, 265339, 265338, 265336, 265335, 265334, 265332, 265309**

This analysis uses the data from these runs with the FAST reconstruction, corresponding to approximately 400 million minimum bias events.

For the majority of the MC studies (MC method test, MC Closure test), the analysis was performed using the standard purpose generated MC production LHC17f2b\_FAST, anchored to the LHC16q\_FAST production. This production consists of around 30 million minimum bias events.

Larger statistics were needed to correct for a pairwise hadron- $\Lambda$  inefficiency due to track merging, which was done using a template created from analyzing the standard purpose generated pp MC production LHC18j2\_FAST, which is anchored to the LHC17q\_FAST production consisting of 15 TeV pp data. This MC production contains around N million minimum bias events.

#### 2.2 Event Selection

Events were selected by requiring a collision Z-vertex of less than 10 cm and at least 3 reconstructed tracks in the event.

This reduces the total number of events (FAST + CENT\_wo\_SDD) considered to approximately 420 million events (see Table ??). The V0A estimator was chosen to determine event multiplicity percentile, and the correlation measurement was performed in three multiplicity percentile bins: **0-20%, 20-50%, and 50-80%**.

Multiplicity	Total Evt.	Has 3 Tracks	$ Z_{vtx}  < 10\text{cm} + 3 \text{ tracks}$	% Pass
0-20%	1.218E08	1.217E08	1.061E08	87.1%
20-50%	1.840E08	1.835E08	1.590E08	86.4%
50-80%	1.850E08	1.804E08	1.563E08	84.5%

**Table 1:** Number of events passing our criteria for each multiplicity bin considered.

For all events, the standard Physics selection with pile-up cuts was applied with `AddTaskPhysicsSelection(kFALSE, kTRUE)`.

## 2.3 Track Selection

### 2.3.1 Associated Hadron Track Cuts

For all associated hadrons, a minimum  $p_T$  cuts of  $p_T > 0.15 \text{ GeV}/c$  was applied. Additionally, an  $\eta$  cut of  $|\eta| < 0.8$  was required. Furthermore, all associated hadrons were required to meet the standard cuts supplied by `AliESDtrackCuts::GetStandardITSTPCTrackCuts2011()` corresponding to track filter bit 1024, with a modified number of `MinNClustersTPC` from the standard cut of 50:

- TPC Refit
- ITS Refit
- **SetMinNClustersTPC: 80**
- `SetMaxChi2PerClusterTPC: 4`
- `SetAcceptKinkDaughters: kFALSE`
- `SetMaxDCAToVertexZ: 2`
- `SetMaxDCAToVertexXYPtDep:  $0.0105 + 0.0350/p_T^{1.1}$`
- `SetDCAToVertex2D: kFALSE`
- `SetMaxChi2TPCConstrainedGlobal: 36`
- `SetRequireSigmaToVertex: kFALSE`
- `SetMaxChi2PerClusterITS: 36`

For the correlation, the associated hadron is selected only in the momentum region

$$1.0 < p_T < 4.0 \text{ GeV}/c,$$

with further binning performed offline.

## 2.4 $\Lambda$ Daughter Proton and Pion Track Cuts

The proton and the pion are required to have a minimum  $p_T$  of  $p_T > 0.15 \text{ GeV}/c$  and an  $\eta$  cut of  $|\eta| < 0.8$ . Furthermore, the proton and pion are required to meet the following quality cuts:

- TPC refit flag enabled
- TPC crossed rows  $> 70$
- $(\text{TPC crossed rows})/(\text{findable clusters}) > 0.8$

All of these cuts are applied to the daughters of the reconstructed  $\Lambda$ , independent of the technique used for said reconstruction. For the correlation, the reconstructed  $\Lambda$  is selected only in the momentum region

$$1.0 < p_T < 4.0 \text{ GeV}/c,$$

with further binning performed offline.

### 2.4.1 Trigger Track Cuts

For the trigger hadron tracks, Hybrid Global constrained tracks were accepted using the cuts supplied by `IsHybridGlobalConstrainedGlobal()`, or track bit 768:

- `SetMinNClustersTPC`: 50
- `SetMaxChi2PerClusterTPC`: 4
- `SetAcceptKinkDaughters`: kFALSE
- `SetMaxDCAToVertexZ`: 3.2
- `SetMaxDCAToVertexXY`: 2.4
- `SetDCAToVertex2D`: kTRUE
- `SetMaxChi2TPCConstrainedGlobal`(36)
- `SetMaxFractionSharedTPCClusters`(0.4)

For the both the di-hadron and h- $\Lambda$  correlation, the trigger hadron is selected in the momentum region:

$$4.0 < p_T < 8.0 \text{ GeV}/c$$

,

with further binning performed offline.

## 3 $\Lambda$ Reconstruction

The  $\Lambda$  candidates were reconstructed through the  $\Lambda \rightarrow p\pi^-$  ( $\bar{\Lambda} \rightarrow \pi^+p$ ) decay channel with a branching ratio of 63.9%. The  $\Lambda$  candidates in this analysis were reconstructed using two separate techniques:

- **V0 Finder Technique** - The V0 finder is a standard method for reconstructing V0s like the  $\Lambda$  within the AliRoot framework. Because of its longer decay length, the V0 finder has no trouble resolving secondary vertices coming from a  $\Lambda$  decay.

## – Resonance Technique –

Kaon candidate tracks are selected from the pool of global AOD tracks with additional wide cuts on  $n\sigma_{TPC}$  and  $n\sigma_{TOF}$  (fig. ??):

$$* |n\sigma_{TPC}| < 3$$

$$* |n\sigma_{TOF}| < 3$$

images/nsigmatof\_track1024.pdf

images/nsigmatpc\_track1024.pdf

**Fig. 1:** N-sigma for Kaons in the TOF (left) and TPC (right) detectors as a function of  $p_T$ . A wide PID cut is used to maximize the  $\phi(1020)$  signal.

images/PIDnsigmaTPCvsTOF.pdf

**Fig. 2:** TOF vs TPC n-sigma distribution for Kaons for the momentum range  $2.0 < p_T^K < 4.0 \text{ GeV/c}$ . Pion contamination is seen in the upper left-hand corner (low TOF nsigma and high TPC nsigma). Tighter PID cuts were tested as a systematic check, but show no significant change in the final correlation distribution (section ??)

Since we have no access to the  $\phi(1020)$  meson directly, the final correlation will include both signal ( $h - \phi$  correlated pairs) and background ( $h - (KK)$  correlated pairs). In order to remove this background,

we need both an estimate of the correlation shape of the  $h - (KK)$  pairs, as well as an estimate of the Signal/Background in the  $\phi(1020)$  mass peak region.

### 3.1 Combinatorial Background Estimation

The Signal/Background can be estimated using a likesign kaon invariant mass distribution, scaled to the integral of the unlike distribution in the mass sideband regions. We run a separate check to make sure the like-sign correctly estimates the underlying background by subtracting the scaled like-sign and perform a standard Voigt plus 2nd order polynomial fit to the remaining  $\phi(1020)$  resonance peak. Doing this shows the residual background to be less than 1% of the total mass peak, so we know that the integral of the scaled like-sign distribution gives us an accurate estimate of the underlying background.



**Fig. 3:** Left: Invariant Mass distribution for un-like sign Kaon pairs (black) for 0-20% Multiplicity Percentile p-Pb collisions. The like sign Kaon pair mass distribution (dashed red) is scaled and used to estimate the combinatorial background under the  $\phi(1020)$  signal. The colored region is the final measurement range  $1.014 < M_{KK} < 1.026$  GeV, accounting for 81% of the total  $\phi$  signal. Right: Corrected un-like sign invariant mass distribution after subtracting the scaled like-sign distribution. The corrected distribution is fit with a Voigt function to capture the resonance peak, as well as a 2nd order polynomial for the residual background. The residual is  $< 1\%$  of the final signal.

### 3.2 Invariant Mass Regions

Since we need to measure the  $h - \phi$  correlation and also estimate the contribution to the correlations from the combinatorial background of non-decay kaon pairs, correlated  $h - (KK)$  pairs were formed with the following invariant mass bins for kaon pairs:

- unlike-sign kaons in  $\phi$  mass region:  $1.014 \text{ GeV}/c^2 < M_{KK} < 1.026 \text{ GeV}/c^2$
- like-sign kaons in  $\phi$  mass region:  $1.014 \text{ GeV}/c^2 < M_{KK} < 1.026 \text{ GeV}/c^2$
- unlike-sign kaons in left sideband region:  $0.995 \text{ GeV}/c^2 < M_{KK} < 1.005 \text{ GeV}/c^2$
- like-sign kaons in left sideband region:  $0.995 \text{ GeV}/c^2 < M_{KK} < 1.005 \text{ GeV}/c^2$
- unlike-sign kaons in right sideband region:  $1.040 \text{ GeV}/c^2 < M_{KK} < 1.060 \text{ GeV}/c^2$
- like-sign kaons in right sideband region:  $1.040 \text{ GeV}/c^2 < M_{KK} < 1.060 \text{ GeV}/c^2$

Correlation background removal was tested with both unlike-sign Sideband regions, as well as with the like-sign correlation distribution in the mass peak region. Within statistical errors, all combinatorial background estimators gave similar correlation structures. Ultimately, an average of the correlation from the unlike-sign kaon pairs in the left and right sidebands was used to estimate the combinatorial background, with the like-sign Kaon pairs being used only for scaling and to check for consistency.

## 4 Correlation Measurement

### 4.1 Full Correlation Measurement Method

The per-trigger correlation is estimated using the formula:

$$C_{trig}(\Delta\phi, \Delta\eta) = \frac{1}{N_{trig}} \frac{B(0,0) * S(\Delta\phi, \Delta\eta)}{B(\Delta\phi, \Delta\eta)} \quad (1)$$

where  $S(\Delta\phi, \Delta\eta)$  is the same event correlation and  $B(\Delta\phi, \Delta\eta)$  is the mixed-event correlation. The properly account for the acceptance effects, the mixed-event distribution is scaled to the value in the  $\Delta\phi = 0$ ,  $\Delta\eta = 0$  bin.

However, with the mass peak cut used for the  $\phi(1020)$  meson, what is actually measured is an angular correlation of  $h - (KK)$  pairs that is comprised of the real  $h - \phi$  signal as well as a background of  $h - (KK)$  pairs. To obtain the true  $h - \phi$  correlation, we must remove the contribution from the random combinatorial Kaon pairs:

$$C_{h-\phi}(\Delta\phi, \Delta\eta) = k_{\text{Signal}} \left( C_{(h-KK)_{\text{Mass Peak}}^{US}}(\Delta\phi, \Delta\eta) - \frac{k_{LS}}{2} * \left[ \frac{1}{N_{Ent}^{LSB}} C_{(h-KK)_{\text{Left SB}}^{US}}(\Delta\phi, \Delta\eta) + \frac{1}{N_{Ent}^{RSB}} C_{(h-KK)_{\text{Right SB}}^{US}}(\Delta\phi, \Delta\eta) \right] \right) \quad (2)$$

Here,  $k_{\text{Signal}}$  accounts for the finite window used for the mass peak, and is calculated using the Voigt function shown in figure ??, and is calculated from the fraction of the signal within our mass peak window ( $\approx 82\%$  for our cuts);  $k_{LS}$  is a scaling factor determined using the like sign invariant mass distribution to scale the un-like sign and like sign distributions to the same values in the invariant mass sideband region  $1.040 < M_{KK} < 1.060$  GeV (fig. ??).  $C_{(h-KK)_{\text{Mass Peak}}^{US}}$  is the correlation of  $h - KK$  pairs within the  $\phi(1020)$  invariant mass peak range (see section ?? for how this mass peak range is selected), while  $\frac{1}{N_{Ent}^{RSB}} C_{(h-KK)_{\text{Right SB}}^{US}}$  is the correlation of  $h - KK$  pairs in the  $\phi(1020)$  mass right sideband region normalized by the number of entries. The two normalized sideband correlations are averaged together to approximate the combinatorial background of random kaon pairs (see section ?? for details of this procedure).


### 4.2 Mixed Event Acceptance Correction

For each multiplicity bin, events were separated into z-vertex position bins with a width of 2 cm, ranging from  $-10$  cm to  $10$  cm. Within each of these multiplicity and z-vertex bins, mixing was performed by filling a pool of all charged hadrons and mixing with the reconstructed KK pairs in a given event (fig. ??).

The mixing pool was chosen to have a track depth of 1000, and the number of files per job was chosen dependent on the multiplicity bin to ensure adequate mixing (fig.??).

Since this analysis relies on three different angular correlations ( $h - h$ ,  $h - \phi$ , and  $h - (\text{like sign } KK)$ ), mixing was performed with the same trigger pool and the three separate associated particles per event.





images/mixed\_USpeak\_mult\_0\_20.pdf

**Fig. 4:** 2D Mixed event h-(US kaon pair) angular correlations for the 0-20% multiplicity bin (all z-vertex bins merged together)

173 After mixing, each of these different correlations are acceptance corrected with their own mixed event  
174 distributions (fig. ?? & ??).

### 175 4.3 Reconstruction Efficiency

176 To estimate the  $\phi(1020)$  reconstruction efficiency, we compare  $\phi$  yields from kaon pair reconstruction to  
177 the true  $\phi$  yields using the MC production LHC17f2b-FAST (anchored to LHC16q-FAST production)  
178 and LHC17f2b-CENT\_wo\_SDD (anchored to LHC16q-CENT\_wo\_SDD production). To calculate the  
179 efficiency, the number of  $\phi$  mesons that decayed to two Kaons which each passed our track selection  
180 criteria was divided by the total number of MC generated  $\phi$  mesons with  $|\eta_\phi| \leq 0.8$  and with daughters  
181 in our acceptance ( $|\eta_K| \leq 0.8$ ).

182 The kaon track selection was separated into two cuts: the standard TPC/ITS track cuts, and the presence  
183 of a matching TOF signal:

$$\mathcal{E}_{\text{Total}} = \mathcal{E}_{\text{TPC}} * \mathcal{E}_{\text{TOFhit}} * \mathcal{E}_{\text{PID}}$$

$$\phi \text{ Track Efficiency} = \frac{(\phi: \text{both daughter K pass Track Cuts})}{(\text{Total } \phi \text{ Produced that decay to KK})} * \frac{(\phi: \text{both daughter K pass Track Cuts + TOF hit})}{(\phi: \text{both daughter K pass Track Cuts})}$$

184 Separating the efficiency in this way allowed for a closer look at the non-uniform acceptance of TOF to  
185 see if this introduced a bias in the final correlation.

186 Efficiencies were calculated as a function of  $p_T$ ,  $\eta$ ,  $\phi$ , Event Z vertex, and Multiplicity. Similarly to  
187 previous efficiency studies in 2013 pPb data, no significant dependency of efficiency on multiplicity was  
188 found (fig. ??). The final efficiency correction was applied as a function of  $p_T$  only.



**Fig. 5:** Plot of the number of tracks in the mixed event pool when mixing took place for the h-(US kaon pairs) angular correlations

In addition to the  $\phi$  reconstruction efficiency, the efficiency for the trigger track cut criteria (Sec. ??) is calculated using the ratio of found triggers to the true trigger yield using the same LHC17f2b MC data. For our associated hadrons, we use the same track cuts as the kaon candidate tracks (Sec. ??), and again calculate the efficiency as the ratio of found hadrons to the true MC hadron yield. Our final pair efficiency is then:

$$\mathcal{E}_{pair} = \mathcal{E}_{trig} * \mathcal{E}_{assoc}$$

The same trigger efficiency used in the pair efficiency is then also to correct our  $N_{trig}$  for our final per-trigger correlation in both the h-h and h- $\phi$  case.


#### 4.4 Removal of Combinatorial K-K Background

Since we have no a priori knowledge of which kaon pairs came from a real  $\phi$  decay, we must remove the contribution to the angular correlation structure due to the combinatorial background of random kaon pairs.

To do this, h-(KK) angular correlations are measured for un-like-sign kaon pairs in two invariant mass sideband regions (fig. ??). The correlation structures in these regions are then normalized and averaged together to give an estimate of the combinatorial background shape. The self-normalized 1D  $\Delta\phi$  correlations in the two sideband regions are shown in figure ??, showing that within statistical fluctuations they have identical correlation shapes.

Next, the h-(LS kaons) angular correlations are measured in the sideband regions, and a scale-factor is calculated to scale the LS and US correlations to the same total integral. This same scale-factor is then used to scale the combinatorial background shape to the proper values, giving the final formula for the combinatorial BG as:

$$\text{Combinatorial BG} = \frac{(h - US_{left}) + (h - US_{right})}{2} * scale \quad (3)$$



images/2D\_uncorr\_hKK.pdf

**Fig. 6:** An example of the same event  $h - (\text{US } KK)$  angular correlation structure before the mixed-event acceptance correction is applied. Plotted is the 0-20% Multiplicity Percentile bin.

In order to understand how the choice of sideband distribution changes the overall correlation structure, the method above was compared to three other methods of estimating the combinatorial background:

- Right US sideband Distribution
- Left US sideband Distribution
- LS Peak region Distribution

In order to visualize the differences of the correlation structure from these methods, the bin-by-bin difference was plotted in units of bin statistical error (fig. ??). The two methods using the different US sidebands show only small difference to the average method used, while the larger differences caused by using the LS method can be mostly attributed to the lower statistics of the like-sign correlations.

Finally, once the combinatorial background is removed (fig. ??), we are left with the full  $h - \phi$  2D angular correlations (fig. ??)


#### 4.5 Full $h - \phi$ and $h - h$ Correlation Measurement

Using Equation ?? (Equation ?? for the di-hadron case) and the efficiencies calculated above, we can plot the 2D and 1D angular correlations for both  $h - \phi$  and  $h - h$  pairs.

## 5 Ratio of Correlated $h - \phi / h - h$ Pairs

### 5.1 Fit of $\Delta\phi$ Correlation Structure

In order to measure the yields within the near- and away-side jet, the angular correlation must first be fit with a function that allows for the separation of jet-like and underlying event components. For this,



images/2D\_corr\_hKK.pdf

**Fig. 7:** An example of the same event  $h - (\text{US } KK)$  angular correlation structure after the mixed-event acceptance correction is applied. Again, plotted here is the single 0-20% Multiplicity Percentile bin.

the 2D correlation function is projected onto  $\Delta\phi$  for the range  $-1.2 < \Delta\eta < 1.2$  due to statistics limiting the ability to fit the full 2D correlation. Several methods were used to estimate the "underlying event" component of the  $\Delta\phi$  correlation (see Section ??). For the 1D fit in  $\Delta\phi$  space, the following fit function was chosen:

$$\text{Fit}(\Delta\phi) = C + A_{\text{near}} * \exp \frac{(\Delta\phi - M_{\text{near}})^2}{2 * \sigma_{\text{near}}} + A_{\text{away}} * \exp \frac{(\Delta\phi - M_{\text{away}})^2}{2 * \sigma_{\text{away}}} + \text{periodicity} \quad (4)$$

where periodicity is taken into account by also including a gaussian with the same parameters as the near and away-side peaks but at offset intervals of  $2\pi$ . Both the  $h - \phi$  and  $h - h$  correlations are fit with this method (fig. ??).

## 5.2 Estimate of Near and Away-side Yields

Once the fit of the 1D  $\Delta\phi$  angular correlations is performed, the constant component of the fit is used to estimate the non-jet yield of correlated pairs. The near-side (away-side) yields are then the integral of the correlation distribution above this fit constant for the  $-\pi/2$  to  $\pi/2$  ( $\pi/2$  to  $3\pi/2$ ) region of  $\Delta\phi$  space (fig. ??).

These yields are calculated for the different multiplicity bins in both the near and away-side peaks, as well as the total yield of correlated pairs for both the  $h - \phi$  and  $h - h$  correlations.

## 5.3 Multiplicity Dependent Ratio Measurement

Performing the same type of fit for the  $h - \phi$  and the  $h - h$  correlations, we are able to measure the ratio of yields of  $\frac{h-\phi}{h-h}$  correlated pairs both in the total event, as well as within the near- and away-side jets (fig.??).



**Fig. 8:** Efficiency vs.  $p_T$  for  $\phi$  meson reconstruction. **Left:** New results for this study using LHC17f2b\_FAST MC dataset anchored to LHC16q\_FAST. **Right:** Old results using 2013 pPb data. There is qualitative agreement between the 2013 and new 2016 calculated efficiency, and in both cases, there is no significant dependence on multiplicity.

Comparing the ratio as a function of multiplicity for the different regions of correlation space, we see that the "Jet-like" yields increase as a function of multiplicity, while the "underlying event" stays relatively flat. Since the overall yield of  $\frac{h-\phi}{h-h}$  is increasing as a function of multiplicity, this suggests that the main cause of the increase in the inclusive pair ratio is due to the increase in the contribution of the "underlying event" to the total yields. Indeed, at 50-80% multiplicity, the total yield is comprised of 70% "underlying event" and 30% "jets", while for the 0-20% multiplicity, the total yield is comprised of 90% "underlying event" and 10% jets (fig. ??).

## 6 Monte Carlo Studies

### 6.1 Correlation Method Test using Monte Carlo

In order to test whether the full correlation measure (eq. ??) accurately describes the real  $h - \phi$  correlation, several Monte Carlo studies were performed. The first of these was a complete test of the correlation extraction method without detector inefficiencies. To accomplish this test, two correlations were measured in MC dataset LHC17f2b\_FAST with the same set of high  $p_T$  ( $4 < p_T < 8 \text{ GeV}/c$ ) trigger hadrons. The first used an associated particle taken from the MC generated  $\phi$  mesons (identified via MC particle's associated PDG code), representing the real  $h - \phi$  correlation. The second used the correlation method described in Section 4 to reconstruct the  $h - \phi$  correlation, using the MC generated Kaons identified via MC particle's PDG code instead of track PID cuts.

Comparing the generated vs. reconstructed correlation in  $\Delta\phi$  shows very good agreement, proving that the background subtraction method using the invariant sideband regions is sound (fig. ??).

### 6.2 MC Closure Test

After the MC method test showed that the general measurement method was correctly recovering the generated  $h - \phi$  correlations, a full MC closure test was performed using LHC17f2b\_FAST and LHC17f2b\_CENT datasets. The generated correlation was taken the same way as the above method test. For the reconstructed case, the full analysis procedure was used including tracking efficiency (Sec. ??). The recon-




**Fig. 9:** Correlations are measured for three different regions of un-like sign Kaon pair Mass: the left sideband, the mass peak region, and the right sideband (colored regions of invariant mass plot). Each of these correlations are separately corrected for acceptance effects using Mixed-Event techniques. The final  $h - \phi$  Correlation is calculated by taking the "mass peak" correlation, and subtracting a scaled average of the two sideband regions.

264 structured  $\Delta\phi$  distribution was then compared to the generated distribution (Fig. ??). A ratio of the two  
 265 distributions fit with a straight line gives a closure of  $0.98 \pm 0.04$ , consistent with 1.

## 266 7 Systematic Errors & Crosschecks

267 For all possible sources of systematic errors, the errors are first calculated per  $\Delta\phi$  bin in the full  $\Delta\phi$   
 268 distribution. This is done using a ratio of all variations to the standard cut and finding the overall RMS  
 269 across all  $\Delta\phi$  bin. After this is done, each variation then undergoes the full yield extraction. The variation  
 270 of the final yields is then calculated again as the RMS of all variations, giving a separate systematic error  
 271 for the near-side, away-side, underlying-event, and total pair yield. For the final  $(h - \phi)/(h - h)$  pair  
 272 ratios, the systematic errors from the individual  $(h - \phi)$  and  $(h - h)$  yields are treated as uncorrelated.



images/SB\_dphicompare.pdf

**Fig. 10:** Self normalized  $\Delta\phi$  correlations for the left and right mass sideband regions, which are averaged together and scaled to estimate the underlying correlation background in the mass peak region.

## 7.1 TOF Efficiency Crosscheck

Since the TOF does not have uniform coverage in  $\phi$  and  $\eta$ , a crosscheck was necessary to ensure that the strict TOF PID signal was not influencing the final correlation measurement. The correlation was performed separately for associated particles that fell in the angular range  $0 < \phi_{assoc} < \pi$  (with gap in TOF coverage), and in the angular range  $\pi < \phi_{assoc} < 2\pi$  (no gap in TOF coverage).

These two correlations were then normalized to 1 to account for the different statistics and plotted against one another. Within statistical errors, there was no difference between the correlations from one side of the detector and the other, showing that there was no effect on the final correlation shape due to the gap in TOF coverage.

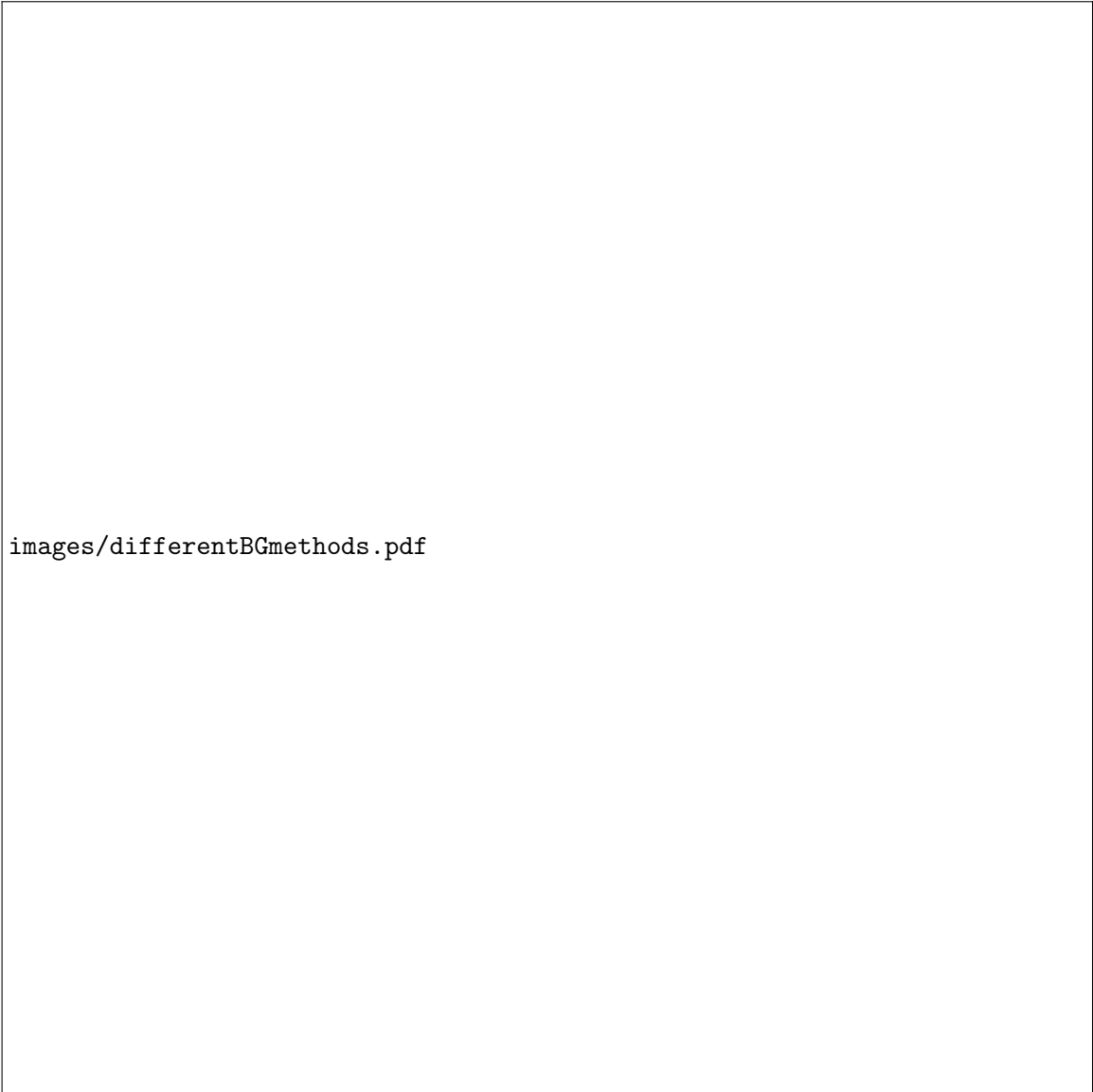
## 7.2 Invariant Mass Range Checks

In order to test the systematic effects of the correlation method (i.e. choosing specific narrow mass regions for the "mass peak", as well as for the "side band" regions for background estimation), it is necessary to vary the width and positions of these regions and see the effect on the final correlation results.

### 7.2.1 Mass Peak Region Check

The mass peak range can be varied by widening and narrowing the  $\phi(1020)$  signal mass region considered. Since this directly changes the Signal/Background of the uncorrected correlation, this variation tests whether or not the Signal/Background of the considered region has an effect on the final correlation even after the fraction of total signal that is excluded is taken into account (i.e. the correlation is corrected by the factor  $k_{\text{Signal}}$  from Eq. ??, which changes with the mass window used).

Within the range variation considered, we see no significant effect on the correlation function (fig. ??) due to the changing Signal/Background ratio. The ratio of each cut to the standard is also plotted, and found to be uniform in  $\Delta\phi$  and consistent with 1. We also project all ratio points for each  $\Delta\phi$  bin onto a single distribution (fig. ??) to find an RMS value of 1.4%, well below the statistical error of the distribution.



images/differentBGmethods.pdf

**Fig. 11:** The bin-by-bin difference in three methods of estimating the combinatorial KK background compared to the averaged US sideband method used in this analysis (plotted in units of sigma i.e. the bin statistical error).

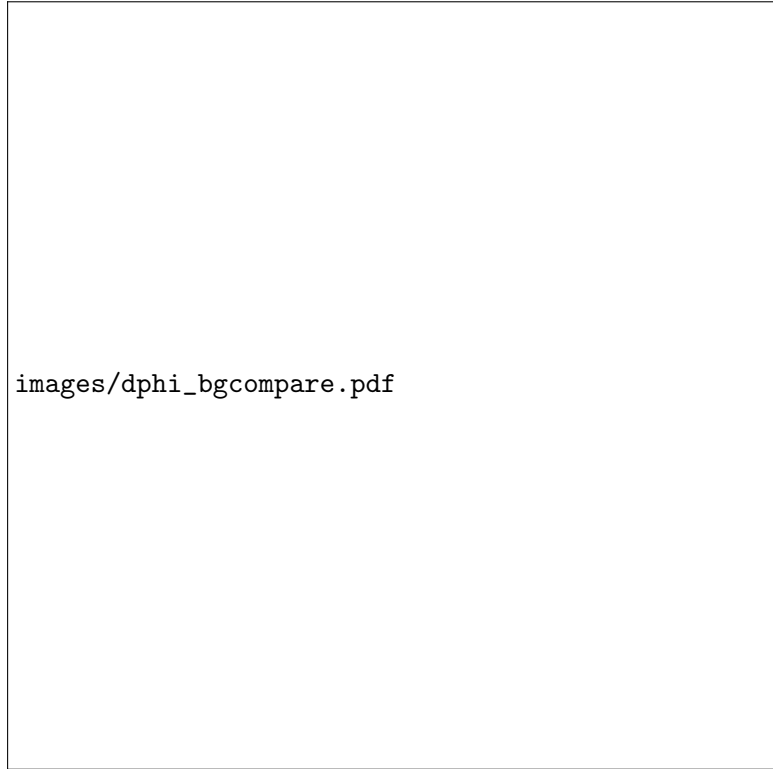
### 7.2.2 Sideband Region Check

The sideband regions of the invariant mass distribution are used for both estimating the correlation background under the mass peak, as well as for the like-sign scaling factor. In order to make sure the choice of sideband region does not significantly change the final correlation structure, both the left and right sideband regions were varied from their standard ranges (fig. ?? & ??). In both cases, variation of the sideband region shows no significant changes to the correlation distribution, with any differences well below the statistical errors of the correlation.

### 7.2.3 Likesign Sideband Scaling Factor Check

To estimate the Signal/Background ratio in the  $\phi(1020)$  mass peak region, the like sign invariant mass distribution is scaled to the integral of the unlike sign sideband regions. Since this scaling factor is influenced both by the statistics of the integral (of both the like and un-like sign distributions), as well as the specific sideband mass ranges, the choice of scaling was varied between the following options:





images/dphi\_bgcompare.pdf

**Fig. 12:** Plotted here is the total  $\Delta\phi$  correlation in the  $\phi$  mass peak region (signal + background), as well as estimated correlation background given by the scaled average of the two sideband regions. Within the mass peak region used for this analysis, the Signal/Background is  $\approx 2.4$

- 310      – Right Sideband only
- 311      – Right Sideband + Statistical Error
- 312      – Right Sideband - Statistical Error
- 313      – Left Sideband only
- 314      – Left Sideband + Statistical Error
- 315      – Left Sideband - Statistical Error
- 316      – Average of Left and Right Sideband
- 317      – Average + Statistical Error
- 318      – Average - Statistical Error

319    The "Average" case is taken to be the central value, and the ratio to the variations to the central correlation  
 320    is plotted as a function of  $\Delta\phi$  (fig. ??). Combining the ratios at each point into a single distribution (fig.  
 321    ??) gives an RMS value of 2%. Since this scaling factor directly shifts the correlation function up or  
 322    down, the variation cannot be ignored even with the larger statistical errors, and must be accounted for  
 323    in the final systematic errors.

### 324    7.3    Correlation Fitting Procedure

325    Since there are several different methods of separating the "underlying event" from the jet peaks in the  
 326     $\Delta\phi$  correlation, a systematic check is needed to see if the final ratios are dependent on the method chosen.

images/2D\_corr\_hPhi.pdf

**Fig. 13:** The final  $h-\phi$  2D angular correlation measurement, after efficiency, mixed event acceptance, and combinatorial BG subtraction. Shown here is the single 0-20% Multiplicity Percentile bin.

The correlation consists of 16 bins in  $\Delta\phi$ , and the underlying event can be estimated by looking at those bins that are farthest from the near and away jet peaks:

- Average of bins 1, 8, 9, 16
- Average of bins 1, 8, 9
- Average of bins 1, 2, 7, 8, 9, 16
- Full Correlation Fit (straight line as free parameter)

For the "Full Correlation Fit", the whole distribution is fit with two gaussians (the near and away-side peaks) and a straight line component. After the full fit converges, only the straight line parameter is extracted and used as the "underlying event".

For our final systematic, we take the RMS value of the distribution of ratios given from each of the listed BG estimation procedures (fig. ??). This gives us the following related systematic for the near-side, away-side, and UE:

Region	0-20% Error	20-50% Error	50-80% Error
near-side	3.2%	5.8%	8%
away-side	8.8%	4.9	7.7%
U.E.	0.7%	0.7%	2%

**Table 2:** Systematic error in percent from the estimation method of our underlying event.

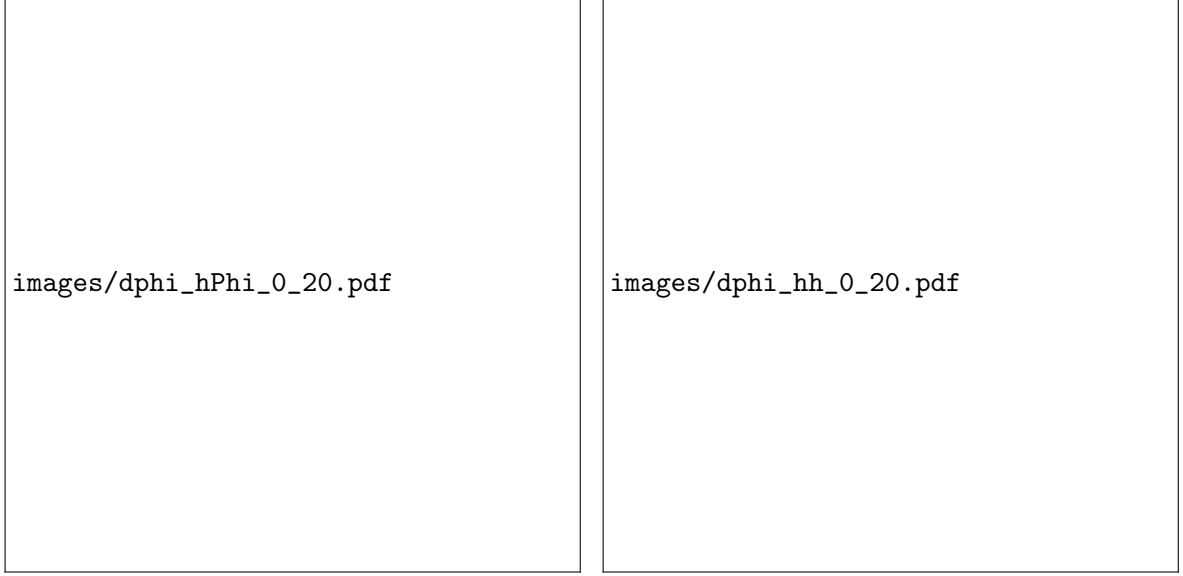


**Fig. 14:** Angular Correlations for  $h - \phi$  (left) and  $h - h$  (right) pairs after full acceptance and efficiency corrections. Both distributions are fit with a function (dashed lines) consisting of two Gaussians and a constant BG term. The constant BG term of the fit is used in calculating the "Jet-like" yields in the near- and away-side peaks.

#### 7.4 PID cuts

With a relatively wide PID cut, we need to check that the inclusion of pion contamination does not effect our final correlation structure. To do this, the TPC PID cut was varied from the standard cut of  $|n\sigma_{TPC} < 3|$  to 2.8, 2.6, 2.4, 2.2 and 2.0.

#### 7.5 Affect of $v_2$ Assumption on Ratios

Since the near and away-side peak (and underlying event) yields are calculated based on the assumption of a flat background underneath the jets, an additional check is needed to see if the inclusion of a  $v_2$  term changes the final  $(h - \phi)/(h - h)$  ratios. Since a published value for  $\phi$   $v_2$  in p-Pb was not available, we chose to use the published values for inclusive charged hadrons to estimate a systematic error. Using the published ALICE values (<https://doi.org/10.1016/j.physletb.2013.08.024>) gives us a  $v_2$  in the 0-20% bin of 0.15, while the 20-50% and 50-80% values are taken as 85% and 50% of the high multiplicity value, respectively.

By computing the pair yields using the non-zero  $v_2$  values, we can compare the effect on the  $(h - \phi)/(h - h)$  ratio measurement to our flat background assumption. Since the  $(h - h)$  and  $(h - \phi)$  correlations are treated with the same charge particle  $v_2$ , the overall effect on the ratio is a slight decrease in the jet yields at high multiplicity. On the other hand, since the non-jet component is so dominant within our correlation momentum ranges, the non-zero  $v_2$  does not have a visible effect on the Underlying Event ratio.



**Fig. 15:** Example histogram showing how the yields in the different regions of correlation space are calculated. The green region represents the "Underlying Event", and is defined by the constant BG term of the  $\Delta\phi$  fit function. The near- (red) and away-side (blue) Jet yields are defined as the area above the constant BG in the  $-\pi/2 < \Delta\phi < \pi/2$  and  $\pi/2 < \Delta\phi < 3\pi/2$  regions, respectively.

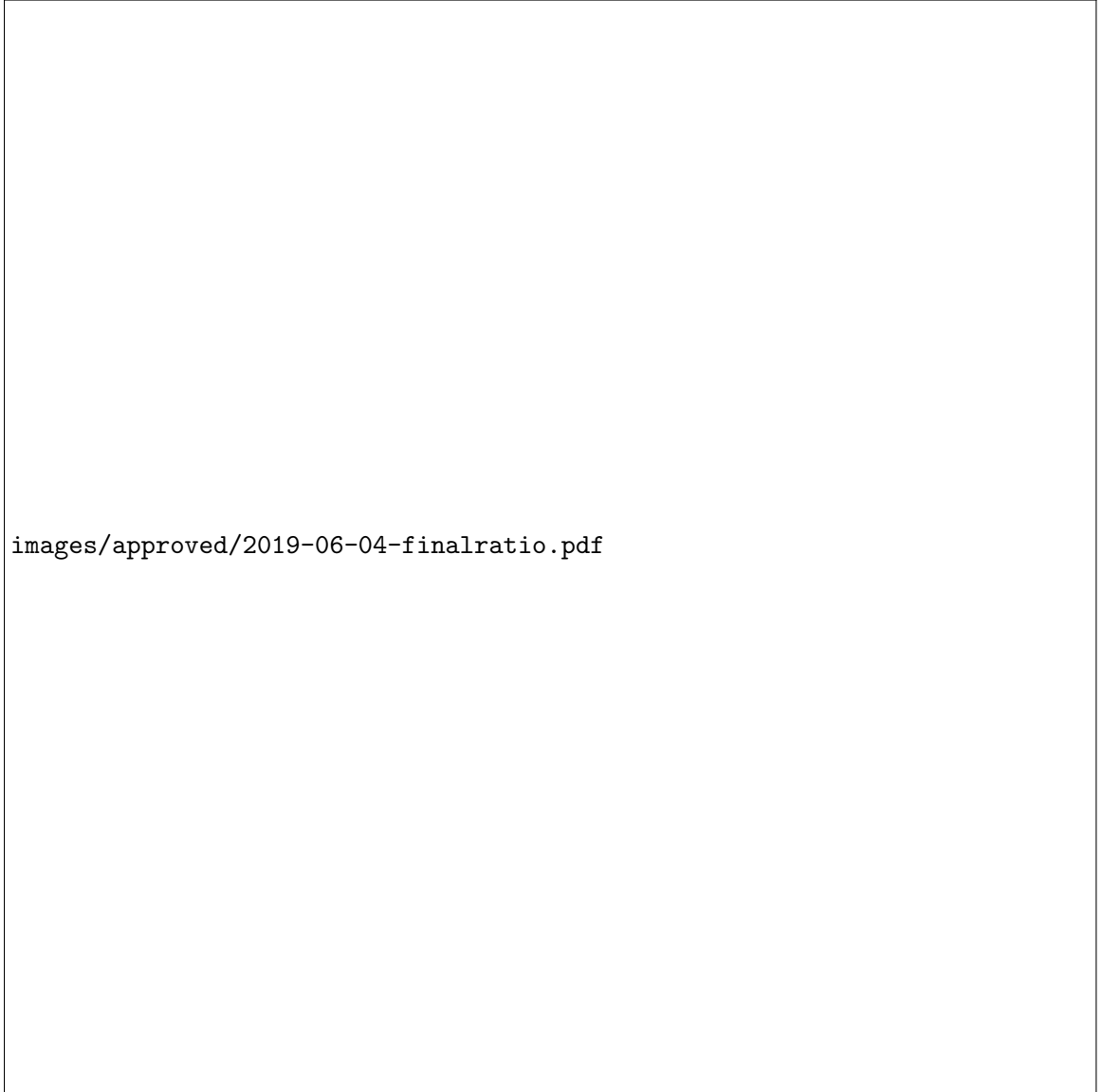


**Fig. 16:** Ratio of the yields of correlated  $\frac{h-\phi}{h-h}$  pairs as a function of multiplicity percentile. Near-side (away-side) yields are calculated by integrating the correlation distribution in the  $-\pi/2$  to  $\pi/2$  ( $\pi/2$  to  $3\pi/2$ ) and subtracting the flat background component of the  $\Delta\phi$  fit. The Underlying Event is estimated using the constant background term directly.



**Fig. 17:** Ratio of the yields of correlated pairs in the Jet peaks to the total number of correlated pairs for both  $h-h$  (orange) and  $h-\phi$  (teal), as a function of multiplicity. This ratio represents the percent of our correlation that is contained in within the near + away-side jets. As we move from low multiplicity to high multiplicity, we see that our jet component represents a smaller fraction of our correlation for both  $h-h$  and  $h-\phi$  pairs.

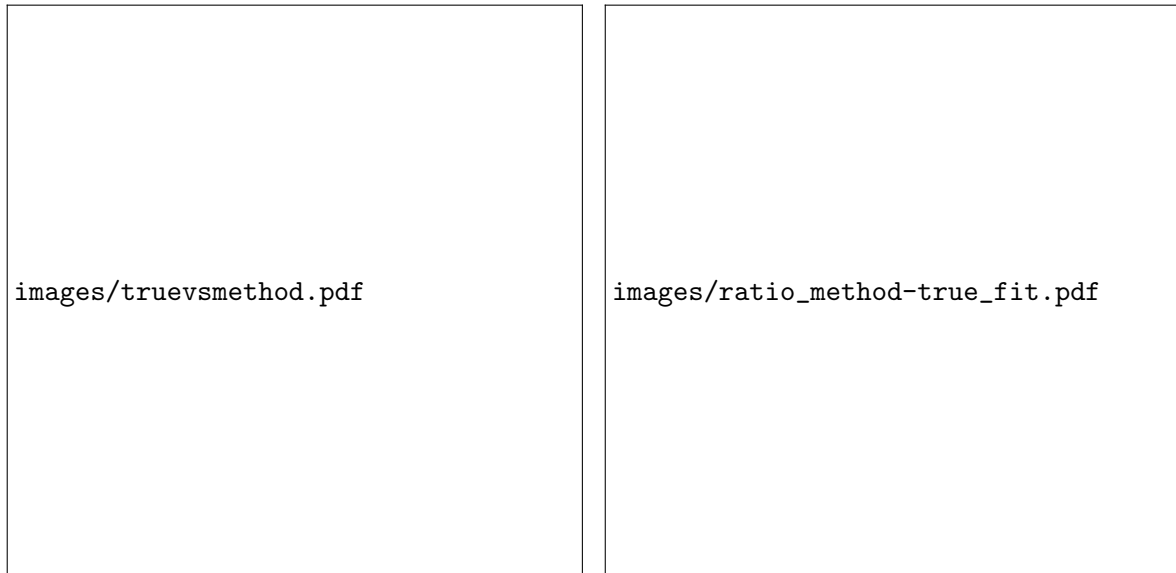


**Fig. 18:** Direct comparison of the generated (green) and reconstructed (red)  $\Delta\phi$  correlation, using the LHC17f2b.FAST dataset (left). The ratio of the two distributions (right) shows that the reconstruction technique in Eq. ?? is able to correctly capture the real  $h-\phi$  correlation, with a straight line fit of the ratio giving a value of  $0.99 \pm 0.02$



**Fig. 19:** Full MC Closure test (**left**) comparing the generated per-trigger correlation (green) with the correlation measured using the track reconstruction outlined in eq. ?? (blue). The ratio of the two (**right**) shows good agreement with 1, within statistical fluctuations.

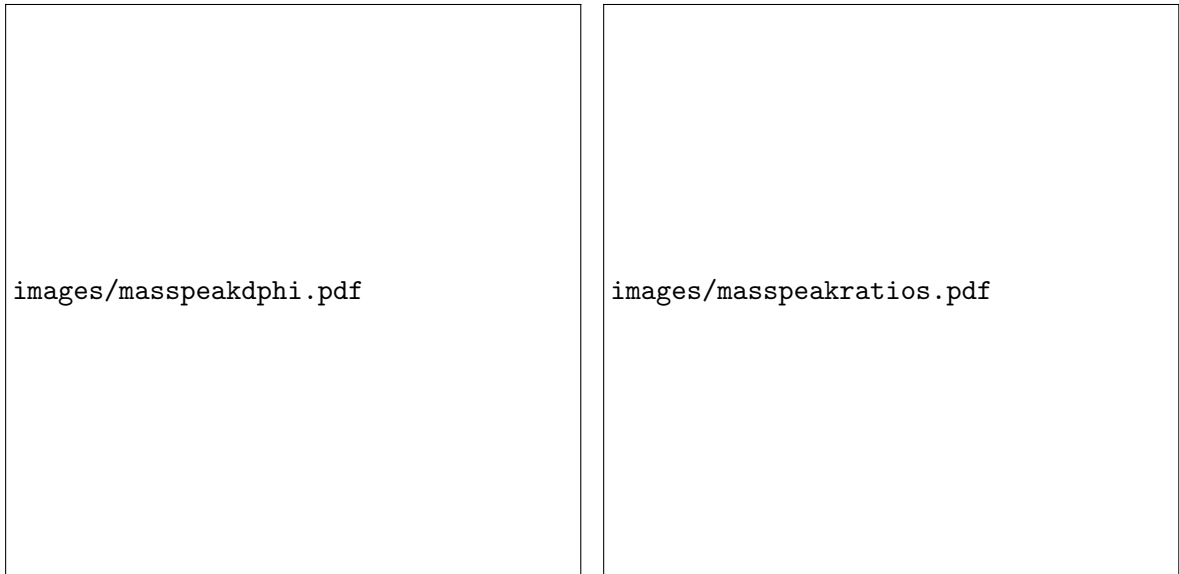


**Fig. 20:**  $\Delta\phi$  correlation (**left**) showing the differences between different invariant mass ranges for the  $\phi(1020)$  signal region. By looking at the ratio of these correlations to the chosen range ( $1.014 \text{ GeV}/c^2 < M_\phi < 1.026 \text{ GeV}/c^2$ )

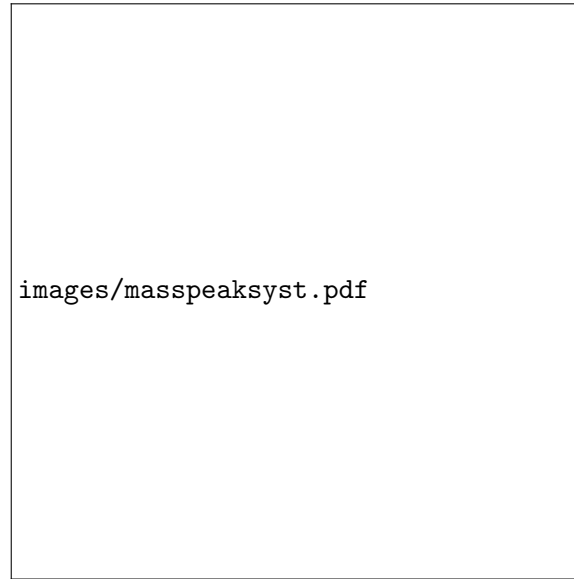



**Fig. 21:**



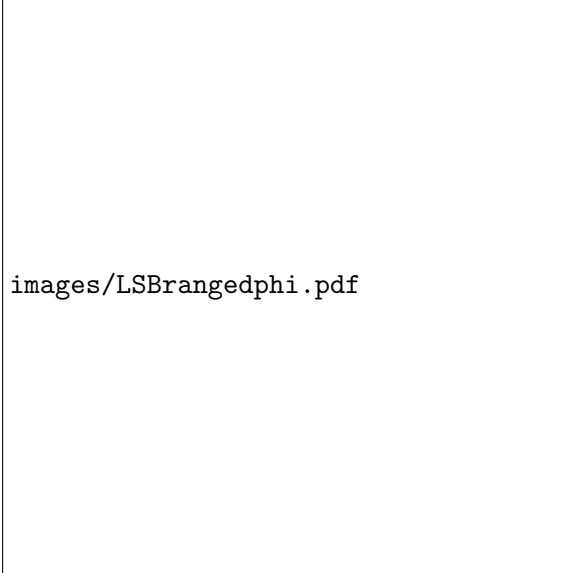
**Fig. 22:** Plot showing the variation in final  $\Delta\phi$  correlation (**left**) from varying the right sideband invariant mass region. This variation changes both the correlation background subtraction, as well as the likesign scaling factor. However, from the ratios of the variation to the standard range (**right**), we see this variation has no effect on the final correlation structure.






images/RSBrangesyst.pdf

**Fig. 23:** Projection of the ratio  $\Delta\phi$  points onto a single distribution shows no significant difference from the variation in right sideband region (RMS of 0.5%)



images/LSBrangedphi.pdf



images/LSBrangeratio.pdf

**Fig. 24:** Plot showing the variation in final  $\Delta\phi$  correlation (**left**) from varying the left sideband invariant mass region. This variation changes both the correlation background subtraction, as well as the likesign scaling factor. However, from the ratios of the variation to the standard range (**right**), we see this variation has no effect on the final correlation structure.



**Fig. 25:** Projection of the ratio of  $\Delta\phi$  points from fig. ?? onto a single distribution shows no significant difference from the variation in left sideband region (RMS of 1.0%)

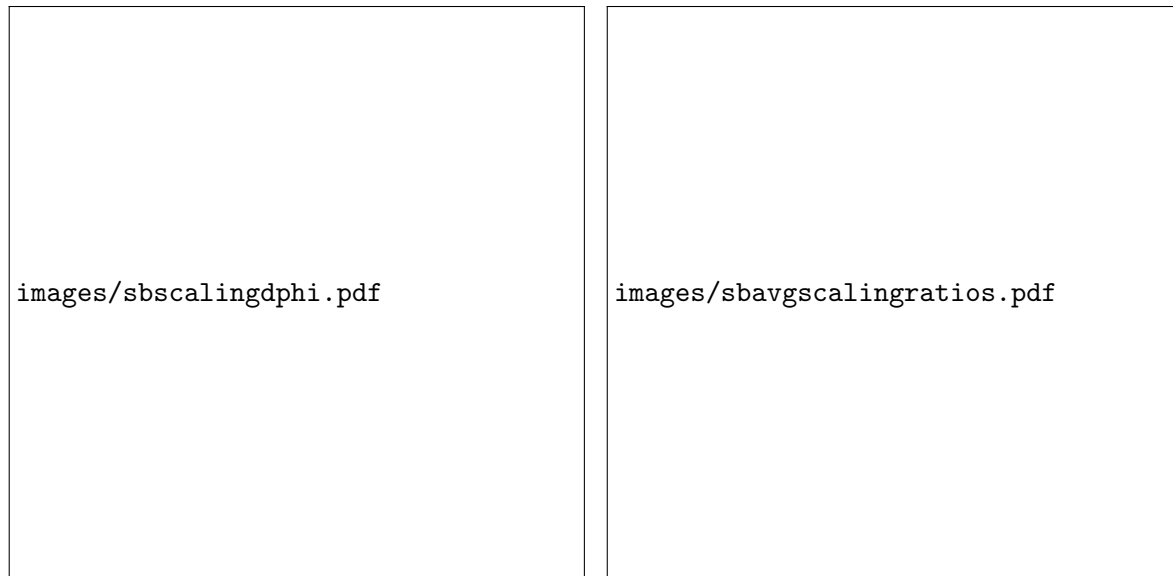
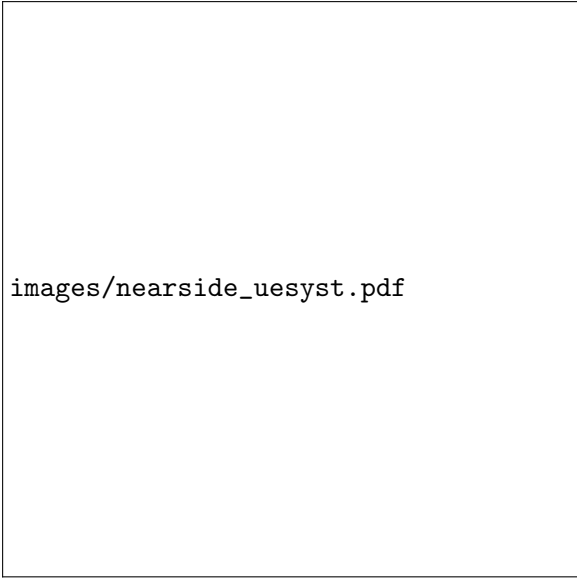


**Fig. 26:** Plot showing the variation in final  $\Delta\phi$  correlation (**left**) from varying the likesign scaling factor, directly changing the Signal/Background estimation. This variation acts to shift the overall correlation up or down.

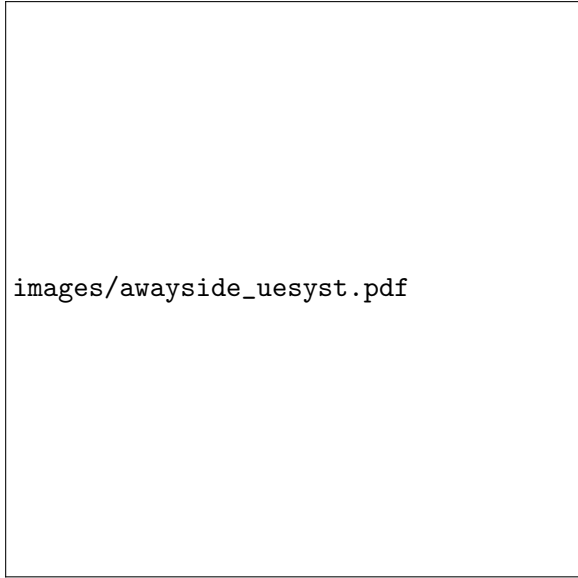


images/sbavgscalingsyst.pdf

**Fig. 27:** Projection of the ratio of all  $\Delta\phi$  points from fig. ?? onto a single distribution shows a variation due to the choice of scaling factor used (RMS of 2.0%)



images/nearside\_uesyst.pdf



images/awayside\_uesyst.pdf

**Fig. 28:** Plot showing the variation in the yield ratios for the different flat background assumptions

## A Second Momentum Bin Measurement

In order to further study the  $\phi(1020)$  production in jets vs. the underlying event, we can also split the associated momentum bin into a high and low  $p_T$  component. This allows us to look at the same measurement in a more jet-dominated regime (higher momentum) and in a more underlying-event dominated regime (lower momentum). For this purpose, we chose the associated momentum bins of  $1.5 < p_T^\phi < 2.5 \text{ GeV}/c$  for the lower bin, and  $2.5 < p_T^\phi < 4.0 \text{ GeV}/c$  for the higher momentum bin. The correlation analysis is performed for these two separate momentum bins exactly as laid out in Section 4, and is done for both  $h$ - $\phi$  and  $h$ - $h$  correlated pairs.

By comparing the ratio of  $(h - \phi)/(h - h)$  pairs in these two different momentum regimes (fig. ?? & ??), we can see that the general trends of an enhanced  $\phi$  production in the Underlying Event, and the increase in  $\phi/h$  production as a function of multiplicity, both hold true. This suggests that these general trends are not influenced by being measured in a more jet-production dominated regime (high momentum) vs. an underlying-event production dominated regime (low momentum).

We also note that the low momentum regime shows a smaller separation between the jet-like production and the underlying event production across all multiplicities. In addition, there is a steeper increase in the ratio within the away-side jet as a function of multiplicity, hinting that jet-medium interactions in the low momentum region may be causing the away-side  $h - \phi/h - h$  ratio to approach the underlying event ratio at high multiplicity (fig. ??).

In looking at the underlying event production, the lower momentum  $h - \phi/h - h$  ratio shows a little increase across multiplicity, while for the higher momentum region, we see a marked enhancement. In both momentum regions, the Total ratio's increase as a function of multiplicity is driven in part by the shrinking jet contribution as multiplicity increases.

## B Jet vs. Total Production comparison

To get a quantitative look at the differences between low multiplicity events (more jet) and high multiplicity events (more underlying event) and the effect this has on the correlation ratios, we can measure the ratio of Jet pairs over Total pairs (i.e. the fraction of correlated pairs that are in a jet) (fig. ??).

From this measurement, there is a clear difference in behavior of jet production of associated  $\phi$  mesons vs. associated inclusive hadrons as multiplicity increases. The fraction of jet-produced hadrons shows a sharp decrease as a function of multiplicity, while the fraction of jet-produced  $\phi$  mesons is significantly lower and flatter as a function of multiplicity. This shows that the balance of production methods of  $\phi$  mesons are mostly independent of multiplicity, while the production methods of hadrons significantly shifts from jet production towards underlying event production as multiplicity increases.

## C Investigating Radial Flow Effects

The two momentum bins chosen show that there is a relatively narrow momentum range (approx.  $2 < p_T < 4 \text{ GeV}/c$ ) that contains sufficient jet production as well as sufficient production in the underlying event to give a statistically meaningful comparison. However, since this ratio is performed in a narrow range, an additional check was performed to look for the effect of radial flow pushing particles into this momentum range as multiplicity increases.

For this purpose, a simple Boltzmann model was chosen to reflect the effect of the radial flow on the spectra of the different particle species:

$$B(p_T) = \frac{C}{T(m+T)} p_T \exp(-(m_T - m)/T) \quad (\text{C.1})$$

where  $m$  is the particle's mass,  $m_T$  is the transverse mass,  $C$  is a scaling parameter, and  $T$  is the free temperature parameter.

For each particle species,  $T$  was found such that the  $\langle p_T \rangle$  for the Boltzmann distribution for a given multiplicity matched with the measured  $\langle p_T \rangle$  previously reported by ALICE (fig. ??).

After fitting the temperatures of the Boltzmann spectra to the measured  $\langle p_T \rangle$ , the spectra were compared between low and high multiplicity regions to see the effect of the increased temperature on production in our chosen momentum region (fig. ??). This shows that the lower mass particles have a larger shift into our momentum region than the  $\phi$  meson, due to the fact that the  $\phi$  has a much higher  $\langle p_T \rangle$  than the other particle species.

From these normalized model Boltzmann Spectra, a ratio is constructed in the  $2 < p_T < 4 \text{ GeV}/c$  region to see the effect this simplified radial flow model would have on the final ratio results (fig. ??). Since the  $\phi$  has a much larger  $\langle p_T \rangle$ , and therefore experiences less of a shift into this region, the overall effect is actually a decrease in the  $\phi/h$  ratio vs multiplicity within this momentum region. As this is the opposite of what we see in the measured  $\phi/h$  ratio, we conclude this effect is not confounded our measurement of strangeness enhancement.

## D Single Trigger Selection and Results

Since the correlation measurement gives per-trigger yields of associated pairs, rather than the associated particles directly, it is possible that event-by-event fluctuations in the number of trigger and associated particles can lead to a small difference between the ratio of associated pairs and associated particles. While the number of events with multiple trigger particles in the defined momentum range  $4 < p_T < 8 \text{ GeV}/c$  is only 12% (and therefore the possibility of discrepancy is limited), an additional crosscheck was performed to look for any effect this had on the final measurement.

For this crosscheck, only a single trigger particle was chosen from each event for the correlation (fig. ??). In events with multiple triggers in the  $4 < p_T < 8 \text{ GeV}/c$ , only the highest momentum trigger was kept. In this way, the correlation measurement is changed from a per-trigger yield to a per-triggered-event yield, with the presence of at least one  $4 < p_T < 8 \text{ GeV}/c$  hadron being the trigger condition.

Dividing the per-trigger measurement by the single-trigger measurement, effects on the final  $\Delta\phi$  correlations is seen to be a flat scale factor across multiplicity. This scale factor for the (h-h) correlation is found to be 1.2, while the (h- $\phi$ ) correlation is essentially unchanged (fig. ??). The slight difference seen in the structure of the (h-h) correlation is caused by the hardening of the trigger spectra (since choosing the highest trigger will skew the trigger momentum).

Since the single trigger analysis acts as a flat scale factor on our original correlation, the effect on our measurement would only be a change of scale on the final  $\phi/h$  ratio. This shows the validity of our method of using standard per-trigger correlations to accurately capture the behavior of the  $\phi/h$  ratio in different production regimes, while also demonstrating the care that needs to be taken when directly comparing this measurement to inclusive  $\phi/h$  yield measurements.

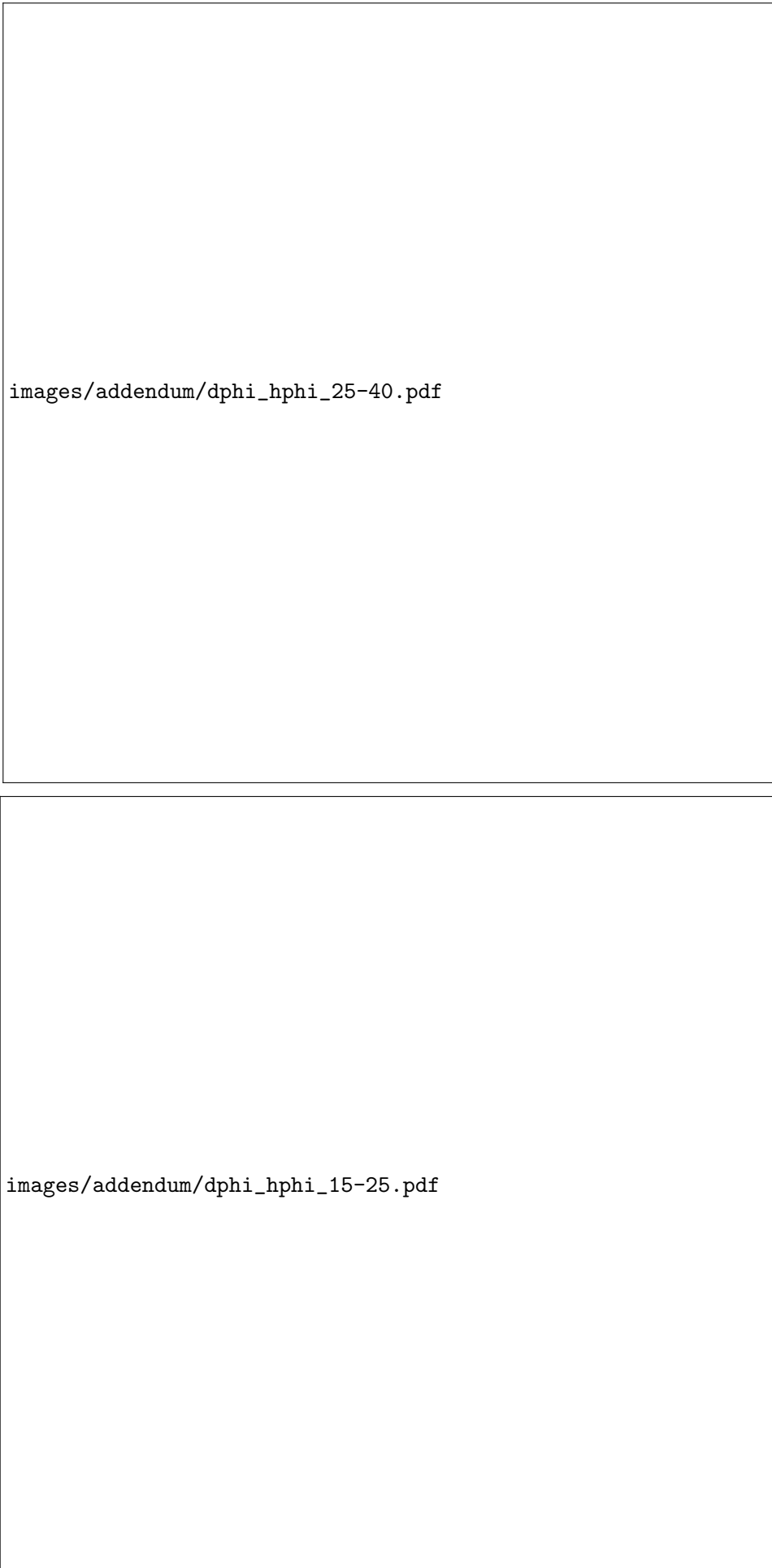
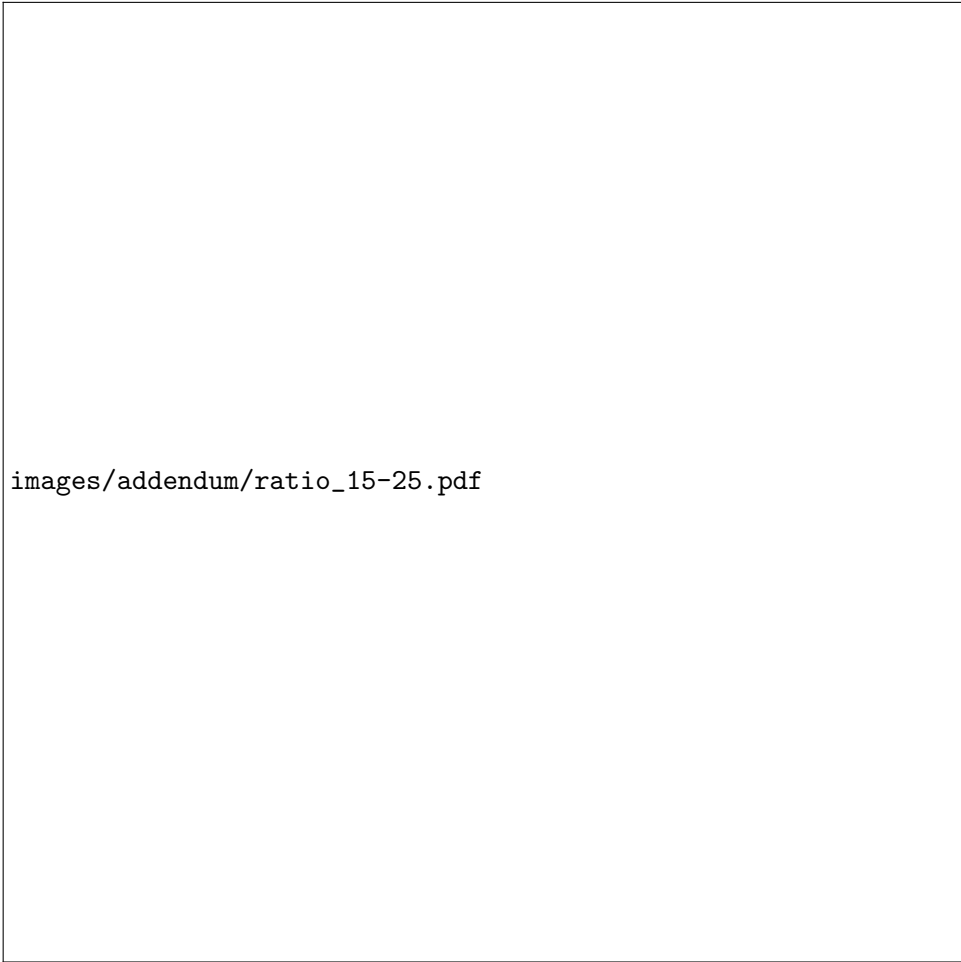



**Fig. A.1:**  $h$ - $\phi$  correlations for both the higher momentum (top) and lower momentum (bottom) regimes, after the underlying event has been subtracted. Jet peaks are structurally similar between the two momentum bins, within

**Fig. A.2:**




images/addendum/ratio\_15-25.pdf

**Fig. A.3:**



images/addendum/jet2totratio\_lowpt.pdf



images/addendum/jet2totratio\_highpt.pdf

**Fig. B.1:** Fraction of Jet Produced correlated pairs as a function of multiplicity for low momentum (left) and high momentum (right) regions. In both momentum regions, the Jet fraction of h-h pairs decreases significantly as a function of multiplicity. For h- $\phi$  pairs, however, the overall fraction coming from jets only slightly decreases as multiplicity increases.






**Fig. C.1:** Temperature of the Boltzmann model for different particle species and multiplicities (left) to match the Boltzmann spectra  $\langle p_T \rangle$  to the published ALICE values (right).



**Fig. C.2:** Boltzmann model spectra comparison between a low and high multiplicity bin for the  $\phi$  (left) and pion (right). While both particles are shifted to high momentum at high multiplicity, the pion sees a much larger increase in the marked  $2 < p_T < 4 \text{ GeV}/c$  region

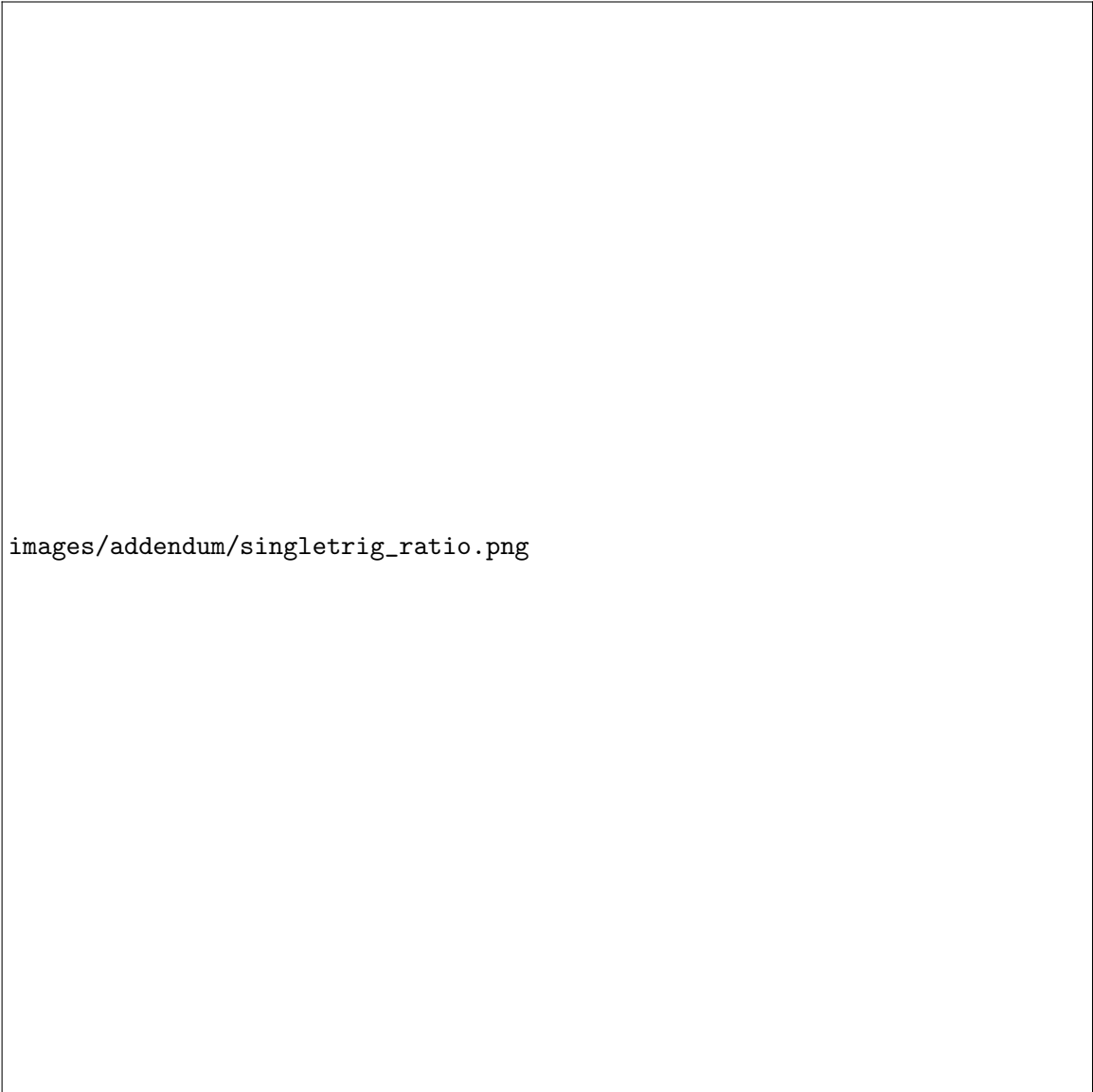


images/addendum/boltz/boltzratio.png

**Fig. C.3:** Normalized ratio of  $\phi$  to stable hadrons vs. multiplicity based on the simplified Boltzmann model fit from measured  $\langle p_T \rangle$  in the region  $2 < p_T < 4 \text{ GeV}/c$ . From the model results, the effect of increased  $\langle p_T \rangle$  would actually decrease the  $\phi/h$  ratio due to the much higher  $\langle p_T \rangle$  of the  $\phi$  compared to the other hadrons.



**Fig. D.1:** Comparison between the standard per-trigger correlation (solid markers) and the highest-trigger correlation (open markers) for the 20-50% multiplicity bin.

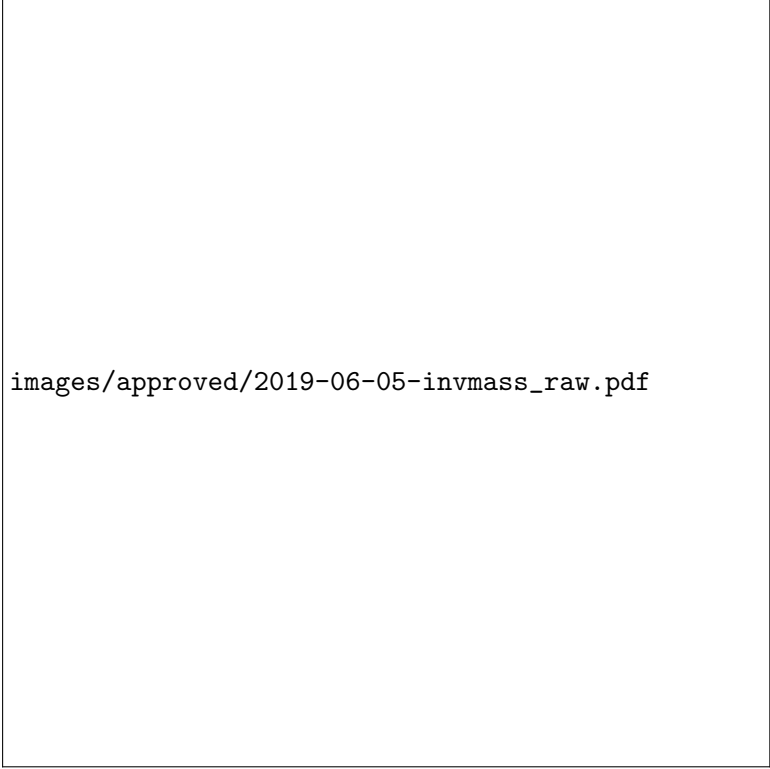


images/addendum/singletrig\_ratio.png

**Fig. D.2:** Ratio of the standard per-trigger correlation to the single-trigger correlation. The effect of choosing a single high trigger is a constant scaling across all multiplicities. Since most events that have a  $\phi$  meson only have a single  $\phi$  meson, the change in trigger scaling has a negligible effect on the  $h - \phi$  correlation.

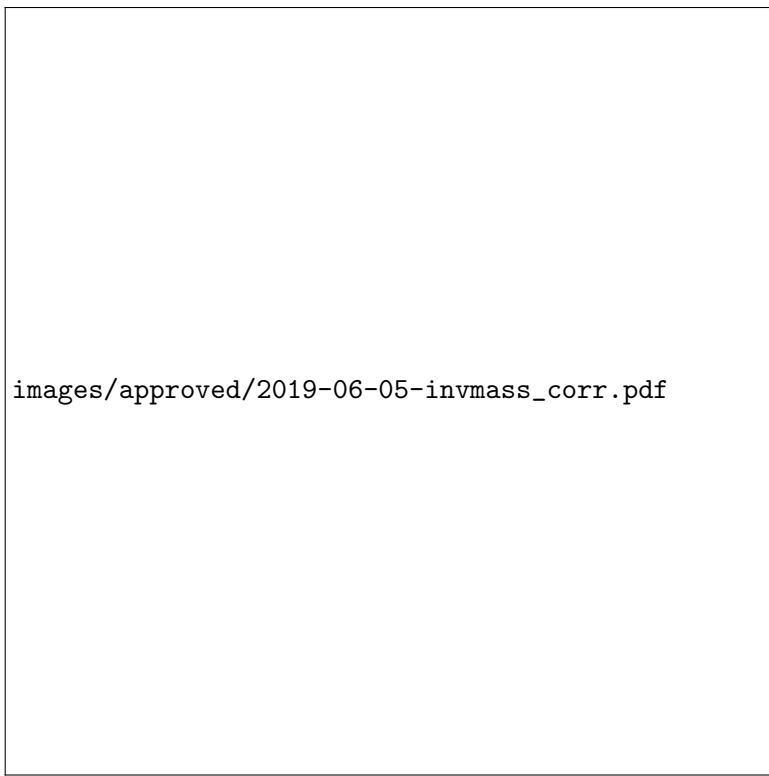
## 432 **E Additional Plots**

### 433 **E.1 Approved Plots**




images/approved/2019-06-05-invmass\_raw.pdf

**Fig. E.1:**



images/approved/2019-06-05-invmass\_corr.pdf

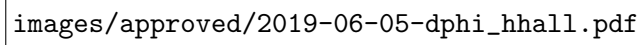
**Fig. E.2:**



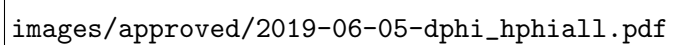
images/approved/2019-06-04-dphi\_bgcompare.pdf

**Fig. E.3:**

**Fig. E.4:**



images/approved/2019-06-05-dphi\_hhall.pdf



images/approved/2019-06-05-dphi\_hphia11.pdf



434 **E.2 Misc. Plots****Fig. E.6:****Fig. E.7:**

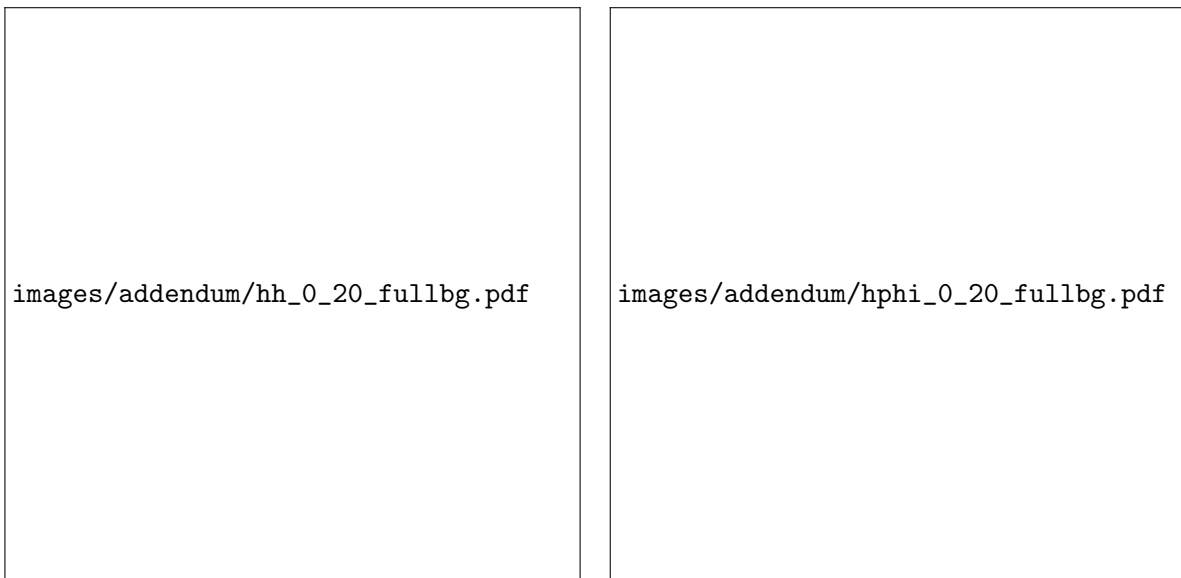


**Fig. E.8:**